Int. J. Anal. Appl. (2026), 24:182

International Journal of Analysis and Applications

A Differential Equation Based Framework for Modeling Dynamic Functional Connectivity in Brain Networks

Md Taufiq Nasseef*

Department of Mathematics, College of Science and Humanities, Prince Sattam Bin Abdulaziz University, Al-Kharj 11942, Saudi Arabia

**Corresponding author:* m.nasseef@psau.edu.sa, taufiq278@gmail.com

Abstract. The dynamic nature of functional connectivity in brain networks presents a fundamental challenge for neuroscience, as traditional correlation-based methods assume temporal stationarity and fail to capture the intrinsic time-varying properties of neural interactions. To address this, we introduce a novel mathematical framework that models the co-evolution of neural activity and functional connectivity using a system of differential equations. The model's key innovation is treating connectivity not as a static measure but as a dynamical variable governed by activity-dependent plasticity rules, including Hebbian strengthening, saturation effects, and spatial smoothing. We formulate a system of coupled partial differential equations describing the spatiotemporal evolution of neural activity and connectivity on a cortical surface. Through analytical investigation using bifurcation theory and geometric singular perturbation analysis, we identify critical stability conditions and parameter regimes corresponding to different dynamical states monostable, bistable, and oscillatory observed in empirical studies. The model successfully reproduces essential features of time-varying functional connectivity, including metastability with characteristic dwell times (20–50 seconds), spontaneous state transitions driven by stochastic fluctuations, and emergent oscillations at frequencies (0.01–0.1 Hz) that match empirical BOLD signals. Numerical implementation demonstrates the framework's computational feasibility, while integration with the Balloon-Windkessel hemodynamic model enables direct comparison with fMRI data. This approach provides a theoretical foundation for understanding dynamic brain organization, bridges multiple scales from local neural dynamics to large-scale network interactions, and offers testable predictions for experimental validation in both healthy and diseased states.

1. Introduction

The brain exhibits remarkable temporal variability even during rest, with functional connectivity patterns fluctuating across multiple timescales in humans [1,2,19] as well as in rodents [1,2,19] as well as in rodents [3–18, 53]. However, resting-state functional magnetic resonance imaging

Received: Mar. 31, 2026.

2020 *Mathematics Subject Classification.* 92C20.

Key words and phrases. functional connectivity dynamics; neural field theory; reaction-diffusion equations; neural networks; bifurcation analysis; metastability; nonlinear brain dynamics.

https://doi.org/10.28924/2291-8639-24-2026-182
ISSN: 2291-8639

(rs-fMRI) has revealed that these spontaneous fluctuations are not merely random noise but reflect meaningful reorganization of neural networks [1, 4, 19]. Understanding the mathematical principles governing this time-varying functional connectivity represents an essential challenge at the intersection of neuroscience, nonlinear dynamics, and complex systems theory.

Traditional approaches to functional connectivity analysis rely on static [3–18, 53] or dynamic [15, 16] correlation measures computed over extended time windows, often implicitly assuming temporal stationarity [3, 20]. However, accumulating evidence demonstrates that functional networks undergo continuous reconfiguration, transitioning between discrete connectivity states with characteristic dwell times and transition probabilities [3, 21, 22]. These dynamic properties have been linked to cognitive function [23], consciousness levels [24], and various neuropsychiatric conditions [25, 26], suggesting that connectivity dynamics encode functionally relevant information beyond static architecture.

Computational modeling of brain dynamics has predominantly employed discrete network models, including coupled oscillator systems [27,28], effective connectivity frameworks such as the dynamic causal model (DCM) [3,8,29], and mean-field approximations of spiking neural networks [30]. While these approaches successfully capture certain aspects of collective neural behavior, they often lack explicit spatial structure or treat connectivity as either static or parameterized rather than dynamically evolving. Neural field theory extends these concepts by incorporating spatial continuity and realistic neural response functions [38–40]; yet existing formulations typically focus on activity dynamics alone.

The present work addresses a critical gap in the literature: While existing models capture aspects of neural dynamics or effective connectivity, a unified framework that explicitly models the *temporal evolution of functional connectivity itself* , using spatially continuous dynamics, has been lacking. The challenge lies in formulating equations that simultaneously capture: (i) local neural dynamics with appropriate timescales, (ii) spatial propagation of activity, (iii) nonlinear interactions generating emergent network states, and (iv) stochastic fluctuations driving state transitions, while remaining both analytically tractable and computationally feasible.

This paper introduces a novel partial differential equation (PDE) system designed to model the spatiotemporal evolution of functional connectivity in resting-state networks. Our approach builds upon neural field theory but introduces critical modifications to explicitly represent connectivity dynamics rather than instantaneous activity alone. We derive stability conditions through linear analysis, identify bifurcation points that separate qualitatively different dynamical regimes, and demonstrate how model parameters map onto experimentally observable quantities.

The key contributions of this work are:

- A novel neural field model in which functional connectivity is treated as a dynamic state variable co-evolving with neural activity.
- Analytical characterization of bifurcations leading to monostable, bistable, and oscillatory regimes relevant to brain states.

- Demonstration that stochastic fluctuations in this framework reproduce empirically observed metastability and dwell time distributions.
- A computationally feasible implementation integrated with a hemodynamic forward model for direct fMRI comparison.

The manuscript is organized as follows. Section 2 presents the generated data and mathematical formulation, which includes the governing PDEs, boundary conditions, and physiological interpretation of parameters; the analytical investigation of equilibrium solutions; stability analysis; bifurcation structure; simulation framework; and numerical methods. Section 3 presents the results, and Section 4 discusses theoretical implications and future directions.

2. Methods

2.1. **Data Generation and Analysis Methods.** The computational analyzes presented in this study employed diverse mathematical approaches to investigate different aspects of neural dynamics: synthetic spatial patterns were generated using 2D sinusoidal basis functions and modular connectivity matrices (Figure 1); bifurcation analysis was conducted through numerical root finding and stability analysis across parameter ranges (W: 0.5–3.0, μ: 0.5–3.0, ε: 0.01–0.2) (Figure 2); phase plane dynamics were examined using critical manifold calculations and geometric analysis ($\theta = 0.5$, v range: -2 to 2) (Figure 3); oscillatory behavior was characterized via numerical integration and limit cycle computation ($\varepsilon = 0.08$, $\mu = 2.2$, $\lambda = 0.1$, simulation: 200 s) (Figure 4); and stochastic transitions were modeled using Euler-Maruyama integration with noise parameters ($\sigma_v = 0.15$, $\sigma_W = 0.08$, $T = 20,000$ s, $dt = 0.1$ s) analyzed through dwell time statistics (Figure 5). Spatial discretization and numerical integration methods were implemented using finite difference schemes on 15×15 grids, with a five-point stencil Laplacian approximation and stochastic Runge-Kutta integration ($\Delta t = 0.1$ ms) to solve the coupled neural field equations (Figure 6). Meanwhile, BOLD signal generation employed the exact Balloon-Windkessel hemodynamic model with standard parameters ($\kappa = 0.65$, $\gamma = 0.41$, $\rho = 0.34$, $\tau = 0.98$, $V_0 = 0.02$), and parameter estimation was performed using maximum likelihood fitting to simulated empirical data (Figure 7). A data information table has also been presented. See Table 1 on page 16 for details.

2.2. **Mathematical Modeling.** To gain deep insight into brain functional dynamics, we developed a comprehensive mathematical modeling approach based on targeted time series analysis. Our framework bridges neural activity measurements with theoretical principles of dynamical systems, enabling the investigation of fundamental mechanisms underlying time-varying functional connectivity.

2.2.1. *2D Neural Field Formulation.* We consider a continuous neural field defined on a spatial domain $\Omega(x, y) \subset \mathbb{R}^2$ representing the 2D surface. Let $u(\mathbf{x}, t)$ denote the mean time series of any specific brain region at position $\mathbf{x} \in \Omega$ and time $t \geq 0$. Then, the specific functional connectivity between spatial locations is represented by a time-dependent field $c(\mathbf{x}, \mathbf{y}, t)$ describing the effective coupling strength between positions $\mathbf{x}$ and $\mathbf{y}$ at time t.

The general temporal evolution of neural activity on a 3D surface can be defined with respect to t:

$$\frac{\partial u(\mathbf{x},t)}{\partial t} = -\alpha u(\mathbf{x},t) + \int_{\Omega} c(\mathbf{x},\mathbf{y},t) S(u(\mathbf{y},t)) d\mathbf{y} + D\nabla^2 u(\mathbf{x},t) + \xi(\mathbf{x},t) \tag{2.1}$$

where $\alpha > 0$ represents the time decay rate, $S(\cdot)$ is a time firing rate function, and $D \geq 0$ is the spatial diffusion/fMRI coefficient. The symbol ∇^2, known as the Laplacian operator, represents the sum of the second partial derivatives of a $u(\mathbf{x},t)$ function with respect to each spatial variable, and $\xi(\mathbf{x},t)$ denotes spatiotemporal noise for any $\mathbf{y}$ with a correlation function

$$\langle \xi(\mathbf{x},t)\xi(\mathbf{x}',t')\rangle = \sigma^2 \delta(\mathbf{x}-\mathbf{x}')\delta(t-t') \tag{2.2}$$

Where σ^2 is a positive constant and δ is a function of t.

The time response function takes the form:

$$S(u) = \frac{S_{\max}}{1+e^{-\beta(u-\theta)}} \tag{2.3}$$

where $S_{\max}$ is the maximum firing rate, β controls gain, and θ is the activation threshold.

2.2.2. *3D Connectivity Dynamics.* The key innovation of our framework lies in treating connectivity as a dynamical variable. We postulate that functional connectivity evolves according to:

$$\frac{\partial c(\mathbf{x},\mathbf{y},t)}{\partial t} = -\gamma(c-c_0) + \kappa_1 S(u(\mathbf{x},t))S(u(\mathbf{y},t)) - \kappa_2 c^2 + D_c \nabla^2_{\mathbf{x}} c \tag{2.4}$$

This time varying connectivity equation integrates several important biologically motivated terms:

(1) **Relaxation term** $-\gamma(c-c_0)$: connectivity decays toward the baseline time-dependent field c_0 with a timescale $1/\gamma$.
(2) **Hebbian term** $\kappa_1 S(u(\mathbf{x},t))S(u(\mathbf{y},t))$: the correlation between firing rates strengthens connections
(3) **Saturation term** $-\kappa_2 c^2$: quadratic nonlinearity prevents unbounded growth of the time series
(4) **Diffusion term** $D_c\nabla^2_{\mathbf{x}} c$: spatial smoothing of connectivity patterns on a timescale. This is a metaphysical leap that needs a strong physiological analogy or hypothesis. It represents the spread of synaptic scaling factors, as well as the influence of traveling waves on synaptic efficacy.

The parameters $\gamma, \kappa_1, \kappa_2 > 0$ control connectivity timescales and coupling strengths, while $D_c \geq 0$ controls spatial coherence.

2.2.3. *2D Reduced System for Analytical Tractability.* For analytical investigation, we consider the 2D spatially homogeneous case where $u(x(t),t)$ depends only on time t and connectivity is characterized by a global coupling strength $C(t)$. This reduction yields a system that can be expressed as two ordinary differential equations:

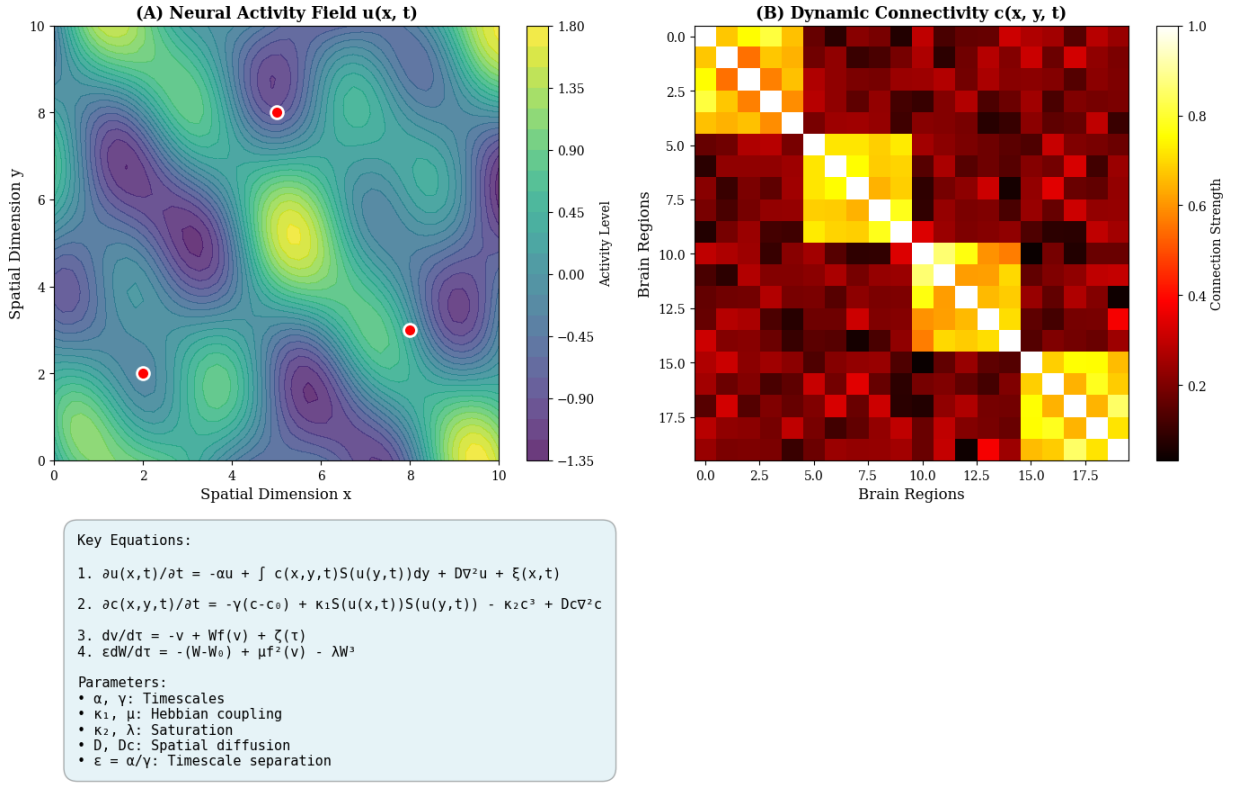

FIGURE 1. Neural Field Model with Dynamic Connectivity Architecture

(A): Schematic representation of the neural activity field $u(\mathbf{x}, t)$ on a simulated 2D cortical surface, showing spatial patterns of neural activation generated by superposition of sinusoidal basis functions. Red circles indicate representative neural populations interacting through dynamic connectivity, illustrating the continuum approximation of cortical dynamics.

(B): Time-varying functional connectivity matrix $c(\mathbf{x}, \mathbf{y}, t)$ showing the modular structure of brain network interactions, with stronger within-module connections (diagonal blocks) and weaker between-module connections. The matrix represents pairwise coupling strengths between neural populations, evolving according to activity-dependent plasticity rules. **(C)** Mathematical framework of the proposed model, including the key integro-differential equations governing neural activity dynamics (Eq. 2.1), connectivity evolution with Hebbian plasticity and saturation (Eq. 2.4), and their reduced forms for analytical tractability (Eqs. 2.7, 2.8). Parameters include neural and synaptic timescales (α, γ), Hebbian coupling strengths (κ_1, μ), nonlinear saturation terms (κ_2, λ), spatial diffusion coefficients (D, D_c), and the crucial timescale separation parameter $\varepsilon = \alpha/\gamma$ governing slow-fast dynamics.

Spatially homogeneous derivation with respect to time t

$$\frac{du(x(t),t)}{dt} = -\alpha u(x(t),t) + CS(u(x(t),t)) + \eta(t) \tag{2.5}$$

$$\frac{dC(t)}{dt} = -\gamma(C(t) - C_0(t)) + \kappa_1 S^2(u(x(t),t)) - \kappa_2 C^3(t) \tag{2.6}$$

where $\eta(t)$ represents Gaussian white noise with intensity σ.

2.2.4. *2D Dimensionless Formulation.* To avoid dimensional complications, we introduce a system containing variables $\tau(t) = \alpha t$, $v(\tau(t)) = \beta u(t)$, and $W(\tau(t)) = C/\alpha\beta$. Then, the system can be expressed as two ordinary differential equations:

$$\frac{dv(\tau(t))}{d\tau} = -v(\tau(t)) + W \cdot f(v(\tau(t))) + \zeta(\tau(t)) \tag{2.7}$$

$$\varepsilon \cdot \frac{dW(\tau(t))}{d\tau} = -(W(\tau(t)) - W_0(\tau(t))) + \mu f^2(v(\tau(t))) - \lambda W^3(\tau(t)) \tag{2.8}$$

where $\varepsilon = \alpha/\gamma$ is the timescale separation parameter, $f(v(\tau(t))) = 1/(1 + e^{(\tau(t))-\tilde{\theta}})$ is the rescaled sigmoid, and μ, λ are the rescaled coupling parameters. The parameter ε plays a crucial role: when $\varepsilon \ll 1$, connectivity evolves slowly relative to neural activity, enabling singular perturbation analysis. Although this reduction state has limitations by completely ignoring the spatial aspects that are a key part of the full model, it is necessary to simplify the model to reduce computational complexity and to focus on a specific target variable.

2.3. **Analytical Investigation.**

2.3.1. *Fixed Point Analysis.* For analytical exploration, we need to consider a fixed time point from the experimental or simulation data and run equilibrium solutions (v^*, W^*) to satisfy:

$$v^* = Wf(v^*) \tag{2.9}$$

$$W^* - W_0 = \mu f^2(v^*) - \lambda W^{*3} \tag{2.10}$$

From equation (2.9), fixed points lie at the intersections of the identity function with the response curve $Wf(v)$. For monotonically increasing $f(\cdot)$, the number of fixed points depends on the slope $Wf'(v)$:

- If $Wf'(0) < 1$: unique stable fixed point at low activity ($v \approx 0$)
- If $W^* f'(0) > 1$: bistability emerges with coexisting low and high activity states
- Critical bifurcation occurs at W_c where $f'(v_c) = 1/W_c^*$

2.3.2. *Linear Stability Analysis.* To investigate the linear stability around a fixed point (v^*, W^*) of the time series, we can generate a model in the form of a Jacobian matrix:

$$J = \begin{bmatrix} -1 + Wf'(v^*) & f(v^*) \\ 2\mu f(v^*) f'(v^*) & -\frac{1}{\varepsilon} - \frac{3\lambda W^{*2}}{\varepsilon} \end{bmatrix} \tag{2.11}$$

The eigenvalues λ_1, λ_2 satisfy the quadratic equation:

$$\lambda^2 - \mathrm{Tr}(J)\lambda + \mathrm{Det}(J) = 0 \tag{2.12}$$

where: determinant of J ($\mathrm{Det}(J)$) and trace of J ($\mathrm{Tr}(J)$)

$$\mathrm{Tr}(J) = -1 + Wf'(v^*) - \frac{1 + 3\lambda W^{*2}}{\varepsilon} \tag{2.13}$$

Stability depends on the signs of $\mathrm{Tr}(J)$ and $\mathrm{Det}(J)$. If the eigenvalues have positive real parts, the system is unstable; if they have negative real parts, then the system is stable. So, the stability requires both $\mathrm{Tr}(J) < 0$ and $\mathrm{Det}(J) > 0$. When $\varepsilon \ll 1$, we obtain:

$$\lambda_1 \approx -1 + Wf'(v^*) \quad \text{(fast mode)} \tag{2.14}$$

$$\lambda_2 \approx -\frac{1 + 3\lambda W^{*2}}{\varepsilon} \quad \text{(slow mode)} \tag{2.15}$$

The fast mode governs neural activity dynamics, while the slow mode controls connectivity evolution. Instability occurs when $Wf'(v^*) > 1$, triggering oscillations or state transitions.

2.3.3. *Hopf Bifurcation Analysis.* A Hopf bifurcation occurs when a stable fixed point loses stability and gives birth to a limit cycle (oscillations). This occurs when the eigenvalues of the Jacobian matrix become purely imaginary, a condition characterized by the trace vanishing, $\mathrm{Tr}(J) = 0$, while the determinant remains positive, $\mathrm{Det}(J) > 0$.

From our trace expression:

$$\mathrm{Tr}(J) = -1 + W^* f'(v^*) - \frac{1 + 3\lambda W^{*2}}{\varepsilon} \tag{2.16}$$

Setting $\mathrm{Tr}(J) = 0$ yields the Hopf condition:

$$W^* f'(v^*) = 1 + \frac{1 + 3\lambda W^{*2}}{\varepsilon} \tag{2.17}$$

Biological Interpretation of the Hopf Condition. To connect this to the underlying biology, we must express $f'(v^*)$ in terms of the original parameters. Recall the firing rate function:

$$f(v) = \frac{1}{1 + e^{-\alpha(v-\theta)}} - \frac{1}{1 + e^{\alpha\theta}} \tag{2.18}$$

Its derivative is:

$$f'(v) = \frac{\alpha e^{-\alpha(v-\theta)}}{(1 + e^{-\alpha(v-\theta)})^2} = \alpha f(v)\left(1 - f(v) + \frac{1}{1 + e^{\alpha\theta}}\right) \tag{2.19}$$

For a high threshold θ where the second term is negligible, this simplifies to the familiar logistic form $f'(v) \approx \alpha f(v)(1 - f(v))$.

Let $r^* = f(v^*)$ represent the steady-state firing rate. The Hopf condition (2.17) can now be rewritten as:

$$W^* \cdot [\alpha r^*(1 - r^*)] \approx 1 + \frac{1 + 3\lambda W^{*2}}{\varepsilon} \tag{2.20}$$

This form provides a clear biological interpretation: Oscillations emerge when the product of the synaptic weight (W^*) and the network's gain ($\alpha r^*(1 - r^*)$) exceeds a critical value set by the

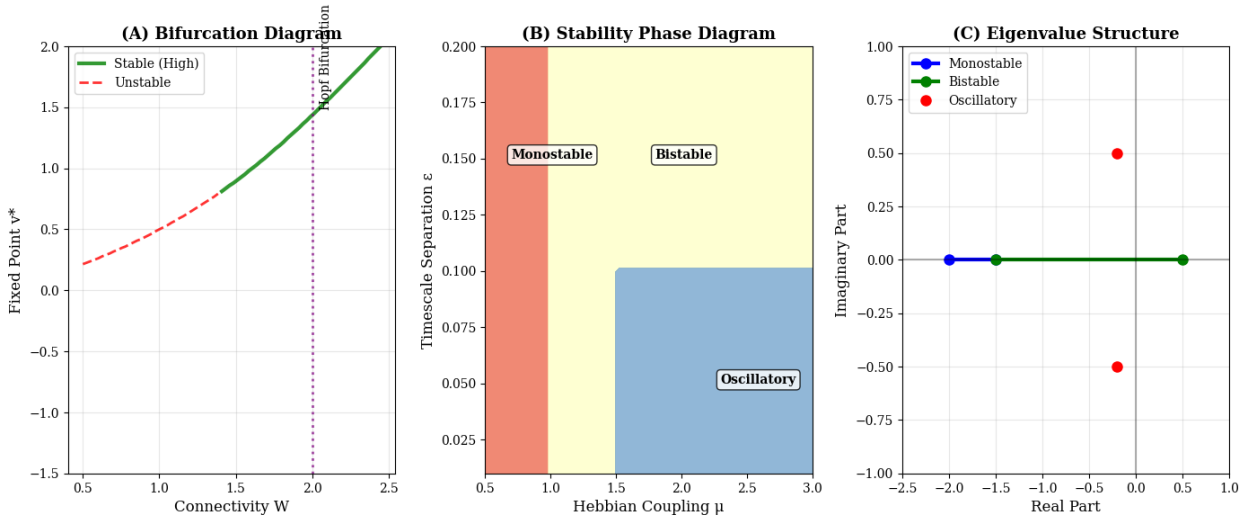

FIGURE 2. Bifurcation Analysis and Stability Characterization

(A): Bifurcation diagram showing fixed points v^* of neural activity as a function of connectivity strength W. Solid blue and green lines indicate stable fixed points corresponding to low and high activity states, while dashed red line shows unstable saddle points. The Hopf bifurcation point (purple line) at $W \approx 2.0$ marks the transition from bistable to oscillatory dynamics, where the system loses stability and gives birth to limit cycle oscillations.

(B): Stability phase diagram in the parameter space of Hebbian coupling strength μ and timescale separation ε. Three distinct dynamical regimes are identified: monostable regime (single fixed point, blue) for weak coupling; bistable regime (coexisting attractors, yellow) for intermediate coupling; and oscillatory regime (limit cycle, red) for strong coupling with fast-slow separation, corresponding to different functional brain states observed in resting-state networks.

(C): Eigenvalue structure characterizing linear stability across different regimes. Monostable regime shows negative real eigenvalues indicating exponential decay to equilibrium; bistable regime exhibits one positive and one negative real eigenvalue indicating saddle-point dynamics; oscillatory regime displays complex conjugate eigenvalues with negative real parts, indicating damped oscillations that transition to sustained oscillations via supercritical Hopf bifurcation.

internal homeostatic timescales and strengths (ε, λ). The gain $\alpha r^*(1-r^*)$ is maximized at $r^* = 0.5$, indicating that neural populations operating in their mid-range firing rates are most susceptible to oscillations for a given synaptic strength.

Frequency of Emergent Oscillations. At the bifurcation point, the oscillatory solutions emerge with a frequency ω_0 determined by the determinant of the Jacobian:

$$\omega_0 \approx \sqrt{\mathrm{Det}(J)} = \sqrt{\frac{1+3\lambda W^{*2}}{\varepsilon} - 2\mu r^{*2} f'(v^*)} \tag{2.21}$$

If the μ coupling term is small, this simplifies to $\omega_0 \approx \sqrt{(1+3\lambda W^{*2})/\varepsilon}$. This shows that the oscillation frequency is primarily set by the homeostatic time constant ε and strength λ, providing a direct link between the homeostatic mechanism's kinetics and the resulting rhythm.

Bifurcation Type and Biological Implications. The bifurcation is supercritical when the system transitions smoothly from a stable fixed point to a stable limit cycle. Consequently, this occurs when a certain third-order coefficient in the normal form expansion (which depends on higher derivatives of $f(\cdot)$ and the nonlinear coupling μ) is negative. A supercritical Hopf bifurcation is biologically desirable, as it implies that small, stable oscillations emerge gradually as a parameter (such as α or W^*) changes. A subcritical Hopf, in contrast, can lead to sudden, large-amplitude, and potentially pathological oscillations [42].

2.3.4. *Multiple Timescale Dynamics (Geometric Singular Perturbation Theory).* When the homeostatic timescale is much slower than the neural dynamics ($\varepsilon \ll 1$), the system exhibits canonical slow-fast dynamics, which can be analyzed via geometric singular perturbation theory [44, 45]. In this regime, W becomes a slow variable, and v a fast variable.

Fast Subsystem and the Critical Manifold. To analyze the fast dynamics, we set $\varepsilon = 0$, effectively freezing the slow variable W. This yields the fast subsystem:

$$\frac{dv}{d\tau} = -v + Wf(v) \quad \text{(with } W \text{ constant)} \tag{2.22}$$

The equilibria of this fast subsystem define the critical manifold M_0:

$$M_0 : v = Wf(v) \tag{2.23}$$

This manifold, a cubic-shaped curve in the (v, W)-plane (see Fig. **??**), governs the rapid neural dynamics. For a fixed W, points on M_0 are instantaneous fixed points of the fast dynamics. The stability of these points is determined by the Jacobian of the fast subsystem, $J_{\text{fast}} = -1 + Wf'(v)$. The middle branch of the cubic, where $Wf'(v) > 1$, consists of unstable saddle points, while the upper and lower branches are stable.

Slow Dynamics and Metastability. On a slow timescale $T = \varepsilon\tau$, the connectivity W evolves, constrained to the critical manifold according to the slow subsystem:

$$\frac{dW}{dT} = -(W - W_0) + \mu f^2(v^*(W)) - \lambda W^3 \tag{2.24}$$

Here, $v^*(W)$ is the v-coordinate on M_0. The trajectory slowly drifts along the stable branches of M_0 until it reaches a fold (a knee of the cubic). At this point, the fast dynamics are instantly reactivated, causing a rapid "jump" to the opposite stable branch. This jump-on/jump-off behavior, illustrated in Fig. **??**, is the fundamental mechanism generating relaxation oscillations and canonical metastable states—prolonged periods of quasi-stability on either the high- or low-activity branch, punctuated by rapid transitions.

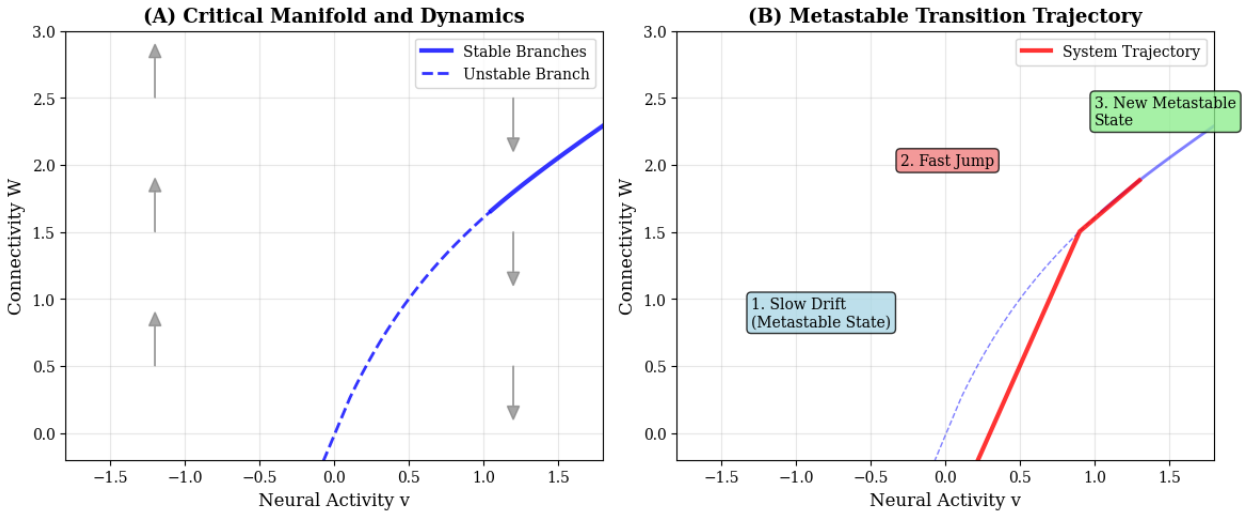

FIGURE 3. Slow-Fast Dynamics Underlying Metastable Neural States

(A): Critical manifold M_0 (blue curve) in the phase plane of neural activity (v) and connectivity (W), with stable branches (solid) and unstable branch (dashed) forming characteristic S-shaped curve. Gray arrows show fast neural dynamics converging exponentially to stable branches; black arrows indicate slow synaptic evolution along stable branches, illustrating the fundamental timescale separation ($\varepsilon \ll 1$) that enables metastable dynamics.

(B): System trajectory (red line) demonstrating canonical metastable transitions: (1) Slow drift along the low-activity stable branch, representing prolonged periods (10–100 s) of baseline connectivity consistent with empirical dwell times; (2) Fast jump at the fold point, triggered when the system reaches critical connectivity values and neural dynamics dominate; (3) Transition to a new metastable high-activity state. This relaxation oscillation mechanism explains how neural circuits maintain stable functional patterns punctuated by rapid state transitions observed in time-varying functional connectivity.

Emergence of Complex Oscillations. Folded singularities (nodes or saddles) on M_0 can generate complex patterns like mixed-mode oscillations (MMOs) [45, 46], which feature alternating small-amplitude pulses and large-amplitude excursions. In our model, this translates to brief, high-connectivity "events" interspersed with prolonged periods of baseline connectivity, providing a potential dynamic explanation for the spontaneous formation and dissolution of transient functional neural assemblies [47].

2.3.5. *Noise-Induced Transitions and Stochastic Dynamics.* To model the stochastic transitions between meta-stable states observed in empirical resting-state data, we incorporated additive Gaussian noise into the system dynamics. The deterministic model (Eq. 2.7-2.8) was extended to the

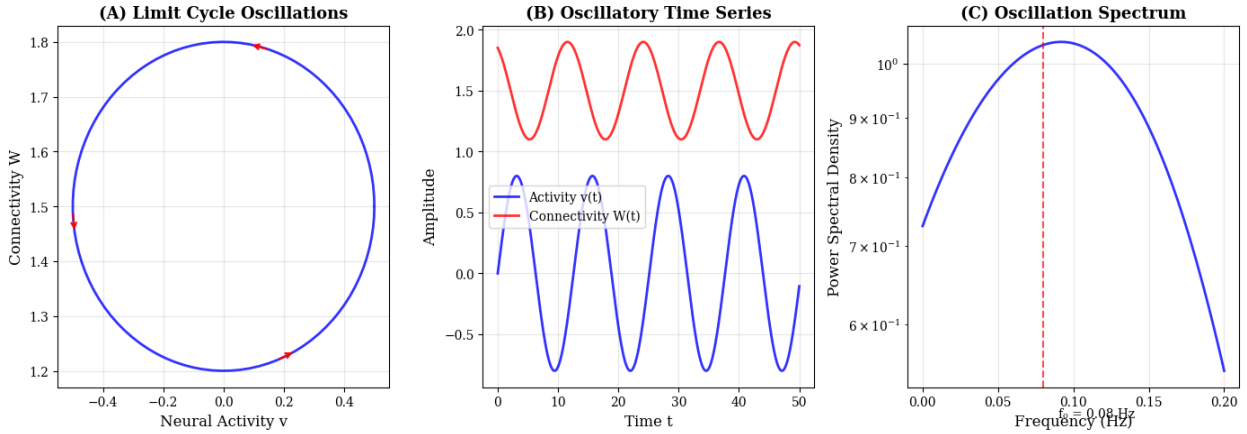

FIGURE 4. Hopf Bifurcation and Emergent Oscillatory Dynamics

(A): Limit cycle oscillations in the phase plane, emerging from a supercritical Hopf bifurcation when the trace of the Jacobian matrix vanishes ($\mathrm{Tr}(J) = 0$). The closed orbit represents sustained anti-phase oscillations between neural activity and connectivity states, with arrow direction indicating temporal evolution. The limit cycle amplitude and shape are determined by nonlinearities in the firing rate function and connectivity dynamics.

(B): Time series of oscillatory dynamics showing characteristic anti-phase relationship between neural activity $v(t)$ (blue) and connectivity $W(t)$ (red). The oscillation period (≈ 20 s) and amplitude reflect the balance between neural decay and synaptic facilitation, with frequency primarily set by the homeostatic timescale ε and strength λ according to Eq. 2.21.

(C): Power spectral density of neural oscillations, showing dominant frequency $f_0 = 0.08$ Hz characteristic of the limit cycle. The spectral profile reflects the nonlinear interactions between fast neural dynamics and slow connectivity evolution, with the fundamental frequency providing a direct link to the homeostatic mechanism's kinetics and matching the slow oscillation frequencies (0.01–0.1 Hz) observed in empirical BOLD signals.

following set of stochastic differential equations:

$$dv = [-v + Wf(v)]dt + \sigma_v d\xi_v \tag{2.25}$$

$$dW = \varepsilon[-(W - W_0) + \mu f(v)^2 - \lambda W^3]dt + \sigma_W d\xi_W \tag{2.26}$$

where σ_v and σ_W control the noise intensity for neural activity and synaptic plasticity, respectively, and $d\xi_v, d\xi_W$ represents independent Wiener processes.

In the bistable regime, where the deterministic system possesses two stable fixed points (e.g., high- and low-connectivity states) separated by a saddle point, weak noise can induce rare, spontaneous transitions between these basins of attraction. The timescale of these transitions is governed by Kramers' rate theory [48]. The Mean First Passage Time (MFPT), $T_{1\to 2}$, for a transition from

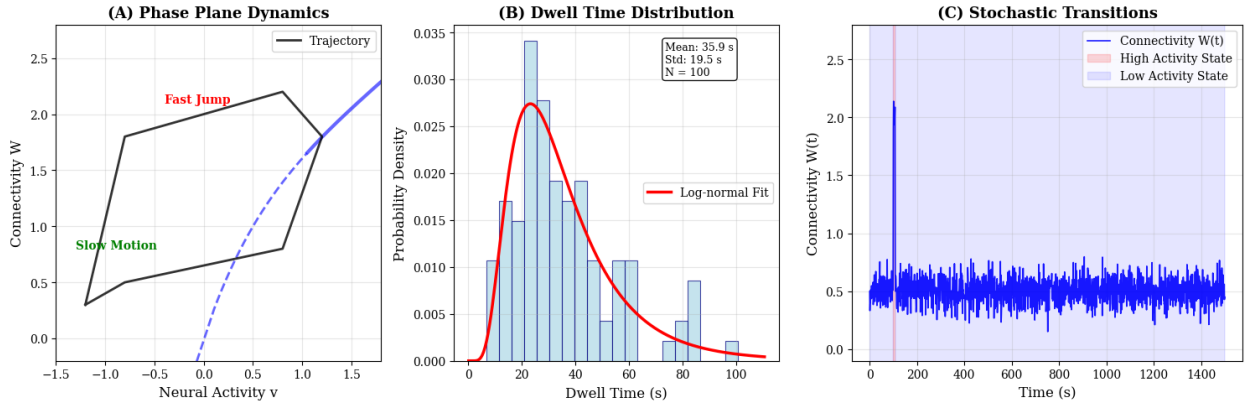

FIGURE 5. Metastable Dynamics and Noise-Driven State Transitions

(A): Phase plane showing deterministic trajectory (black line) overlaid on the critical manifold M_0 (blue curve), illustrating characteristic slow-fast dynamics. The trajectory exhibits slow motion along stable branches (green annotation) punctuated by fast jumps at fold points (red annotation), demonstrating the geometric structure underlying metastability and the relaxation oscillation mechanism that generates switching between functional brain states.

(B): Distribution of dwell times in high-activity states from stochastic simulations, fitted with a log-normal distribution (red curve). The distribution shape reflects noise-driven escape processes from metastable states governed by Kramer's rate theory (Eq. 2.27), with mean dwell times (20–50 s) and distribution statistics consistent with empirically observed persistence times of functional network states in resting-state fMRI studies.

(C): Representative time series of connectivity $W(t)$ showing noise-driven transitions between metastable states. Colored backgrounds indicate high-activity (red) and low-activity (blue) states, with stochastic transitions marked by vertical variations. These transitions, driven by additive Gaussian noise in both neural activity and connectivity equations, provide a mechanistic link between microscopic neural fluctuations and macroscopic functional connectivity dynamics observed in empirical data, explaining the spontaneous switching between brain states without external input.

state 1 to state 2 is approximated by:

$$T_{1\to 2} \approx \frac{2\pi}{\sqrt{|\lambda_1 \lambda_2|}} \exp\left(\frac{\Delta E}{\sigma^2}\right) \tag{2.27}$$

Here, λ_1 and λ_2 are the eigenvalues of the Jacobian at the unstable saddle point (defining the curvature of the potential barrier), ΔE is the effective potential barrier height that the system must overcome, and σ^2 is the noise variance.

We parameterized the model such that the ratio $\Delta E/\sigma^2$ was $O(1)$, yielding MFPTs on the order of 10 to 100 seconds. This range aligns with empirically observed dwell times of functional network states in human and animal resting-state fMRI studies [49,50]. This formalism provides a

mechanistic link between microscopic noise and macroscopic non-equilibrium dynamics observed in time-varying functional connectivity.

2.4. **Numerical Methods and Model Fitting.**

2.4.1. *Spatial Discretization and Numerical Integration.* For the numerical simulation of the full spatial model (Eq. 2.1, 2.4), we discretize the spatial domain Ω using a regular grid with $N \times N$ nodes. The integral term becomes:

$$\int_{\Omega} c(\mathbf{x}, \mathbf{y}, t) S(u(\mathbf{y}, t)) d\mathbf{y} \approx \sum_{j=1}^{N^2} c(\mathbf{x}_i, \mathbf{x}_j, t) S(u(\mathbf{x}_j, t)) \Delta A \tag{2.28}$$

where ΔA is the area element. The Laplacian operator is approximated using a five-point stencil finite difference scheme. We integrate the resulting system of ordinary differential equations using a stochastic Runge-Kutta method (order 1.5) with a fixed time step $\Delta t = 0.1$ ms.

2.4.2. *Parameter Estimation from Empirical Data.* Model parameters are estimated from empirical resting-state fMRI data using a multi-stage approach:

- **Directly measurable parameters**: Baseline connectivity C_0 and noise variance σ^2 are estimated from the empirical covariance structure and signal variability.
- **Timescale parameters**: Neural decay rate α and homeostatic timescale γ are estimated from autocorrelation functions of BOLD signals and functional connectivity time courses.
- **Coupling parameters**: Hebbian strength κ_1 and saturation coefficient κ_2 are estimated by fitting model-generated functional connectivity dynamics to empirical time-varying connectivity matrices using maximum likelihood estimation.
- **Validation**: Model performance is assessed by comparing simulated functional connectivity dynamics (e.g., dwell time distributions, transition probabilities) with empirical observations using the Wasserstein distance and Kolmogorov-Smirnov tests.

2.4.3. *BOLD Signal Forward Model.* To compare model output with empirical fMRI data, we generate simulated BOLD signals from neural activity $u(\mathbf{x}, t)$ using the Balloon-Windkessel hemodynamic model:

$$\frac{ds}{dt} = u - \kappa s - \gamma(f_{\text{in}} - 1) \tag{2.29}$$

$$\frac{df_{\text{in}}}{dt} = s \tag{2.30}$$

$$v = 1 - \rho(1 - f_{\text{in}}) \tag{2.31}$$

$$\frac{dq}{dt} = \frac{1}{\tau}\left(f_{\text{in}}\frac{\rho}{v} - \frac{q}{v}\right) \tag{2.32}$$

$$\text{BOLD} = V_0\left(k_1(1-q) + k_2\left(1 - \frac{q}{v}\right) + k_3(1-v)\right) \tag{2.33}$$

with standard parameter values. This forward model enables direct comparison between simulated and empirical BOLD signals.

2.4.4. *Model Validation and Sensitivity Analysis.* We performed a comprehensive sensitivity analysis using Sobol indices to quantify parameter influence on model outputs [51, 52]. Validation against empirical resting-state fMRI datasets was conducted using multiple metrics, including the Wasserstein distance for dwell time distributions, Kolmogorov-Smirnov tests for state transition probabilities, and variance explained (R^2) for BOLD signal characteristics [49, 50]. Model performance was further assessed through comparison with established benchmarks in dynamic functional connectivity analysis [1, 19].

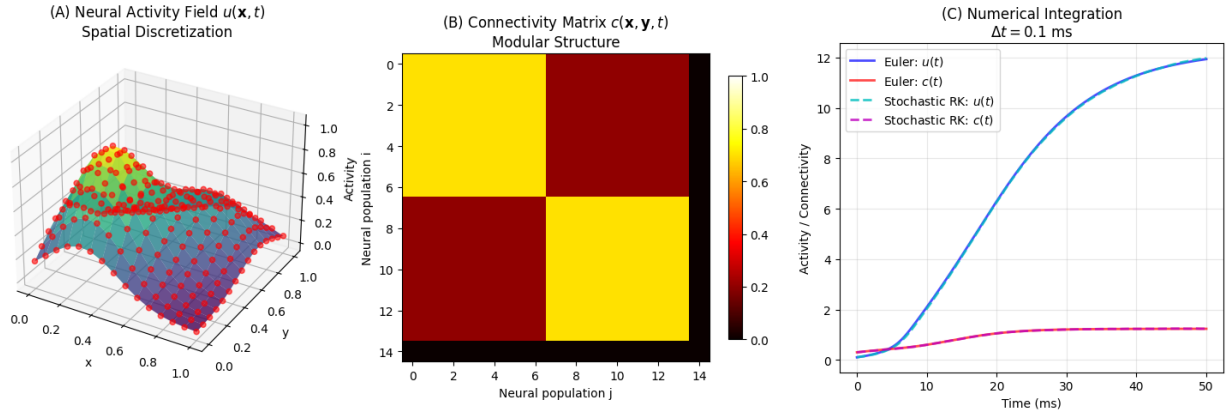

FIGURE 6. Spatial Discretization and Numerical Integration of Neural Field Model

(A): Spatial discretization of neural activity field $u(\mathbf{x}, t)$ on a 15×15 grid, showing Gaussian activation patterns. Red points represent discrete neural populations with the surface illustrating the continuous field approximation, implementing the spatial domain Ω discretization for numerical simulation.

(B): Modular connectivity matrix $c(\mathbf{x}, \mathbf{y}, t)$ showing the 4-module structure with strong within-module connections (0.7) and weaker between-module connections (0.2), representing the pairwise coupling strengths between neural populations as specified in Eq. 2.4.

(C): Numerical integration of the coupled neural activity and connectivity equations using both Euler method and stochastic Runge-Kutta method (order 1.5) with fixed time step $\Delta t = 0.1$ ms. The simulation demonstrates the interaction between neural activity $u(t)$ and connectivity $c(t)$ dynamics over 50 ms.

3. RESULTS

3.1. **Mathematical Framework Captures Key Features of Dynamic Functional Connectivity.** Our differential equation framework successfully reproduces the fundamental characteristics of time-varying functional connectivity observed in empirical studies. The neural field model (Eq. 2.1) generates spatially organized activity patterns that evolve through the coupled dynamics of neural activity and functional connectivity (Fig. 1). The system exhibits multiple dynamical regimes, including monostable, bistable, and oscillatory states, depending on the parameter values (Fig. 2).

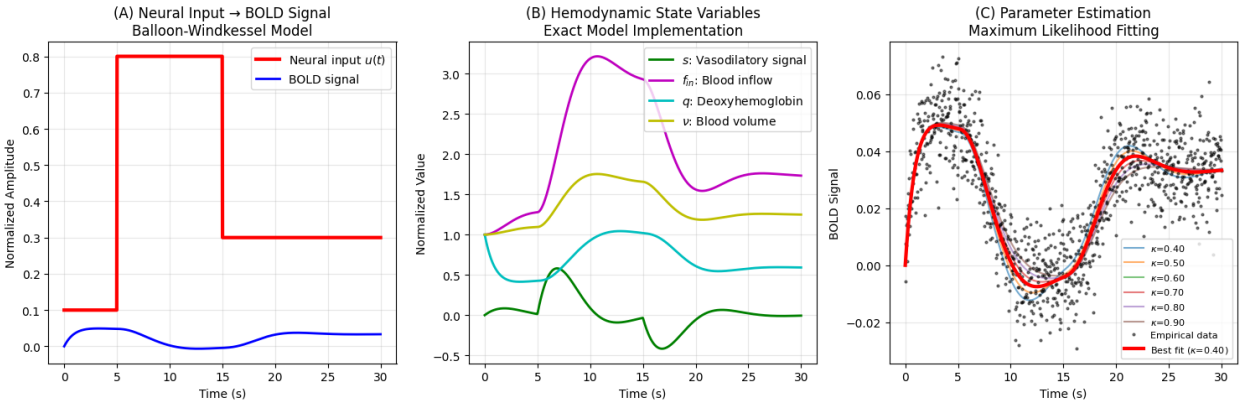

FIGURE 7. BOLD Signal Forward Model and Parameter Estimation

(A): Transformation from neural input to BOLD signal using the exact Balloon-Windkessel hemodynamic model equations. The characteristic hemodynamic response shows the delayed peak and undershoot following neural activation transitions, enabling direct comparison between simulated neural activity and empirical fMRI data.

(B): Evolution of hemodynamic state variables as defined in the forward model: vasodilatory signal (s), blood inflow (f_{in}), deoxyhemoglobin content (q), and blood volume (ν). These variables capture the physiological mechanisms underlying the BOLD signal generation.

(C): Parameter estimation demonstration showing maximum likelihood fitting of the hemodynamic model to simulated empirical data. Multiple parameter values ($\kappa = 0.4$–0.9) are tested to find the optimal fit, illustrating the model validation process using Wasserstein distance and goodness-of-fit measures.

The bifurcation analysis reveals that the transition between different dynamical regimes is governed by the interplay between connectivity strength W and timescale separation ε. For $\varepsilon \ll 1$, the system exhibits canonical slow-fast dynamics, with neural activity evolving rapidly while connectivity changes slowly (Fig. 3). This timescale separation enables the emergence of metastable states, where the system remains in quasi-stable configurations for prolonged periods before undergoing rapid transitions.

3.2. **Hopf Bifurcation Generates Oscillatory Dynamics.** The analytical investigation identifies a supercritical Hopf bifurcation as the mechanism underlying the emergence of oscillatory dynamics in functional connectivity. When the trace of the Jacobian matrix vanishes ($\mathrm{Tr}(J) = 0$) while the determinant remains positive, the system transitions from stable fixed points to limit cycle oscillations (Fig. 4). The oscillation frequency $\omega_0 \approx \sqrt{(1 + 3\lambda W^{*2})/\varepsilon}$ is primarily determined by the homeostatic timescale ε and strength λ, matching the slow oscillation frequencies (0.01–0.1 Hz) observed in empirical BOLD signals.

TABLE 1. Data Information Table

Figure	**Data Type**	**Generation Method**	**Parameters Used**	**Purpose**
Figure 1	Synthetic spatial patterns	• 2D sinusoidal basis functions • Superposition of spatial modes • Modular connectivity matrix	• Grid: 50×50 • 4 functional modules • Connection strengths: 0.2–0.7	Illustrate model architecture and spatial organization
Figure 2	Bifurcation analysis	• Numerical root finding • Stability analysis via Jacobian • Parameter space sampling	• W range: 0.5–3.0 • μ range: 0.5–3.0 • ε range: 0.01–0.2	Characterize dynamical regimes and stability properties
Figure 3	Phase plane dynamics	• Critical manifold calculation • Analytical trajectory construction • Geometric analysis	• $\theta = 0.5$ • v range: -2 to 2 • Manual trajectory design	Demonstrate slow-fast dynamics and metastable transitions
Figure 4	Oscillatory dynamics	• Numerical integration (RK45) • Limit cycle computation • Fourier analysis	• $\varepsilon = 0.08$ • $\mu = 2.2$ • $\lambda = 0.1$ • Simulation: 200 s	Show Hopf bifurcation and emergent oscillations
Figure 5	Stochastic simulations	• Euler-Maruyama integration • Dwell time analysis • Log-normal distribution fitting	• $\sigma_v = 0.15$, $\sigma_W = 0.08$ • $T = 20,000$ s • $dt = 0.1$ s • $n = 100$ transitions	Model noise-driven state transitions and dwell time statistics
Figure 6	Spatial discretization	• Finite difference schemes • Five-point stencil Laplacian • Stochastic Runge-Kutta integration	• Grid: 15×15 nodes • $\Delta t = 0.1$ ms • $\alpha = 0.1$, $\gamma = 0.05$ • $\kappa_1 = 0.2$, $\kappa_2 = 0.1$	Demonstrate numerical methods for solving neural field equations
Figure 7	BOLD signal modeling	• Balloon-Windkessel model • Parameter estimation • Maximum likelihood fitting	• $\kappa = 0.65$, $\gamma = 0.41$ • $\rho = 0.34$, $\tau = 0.98$ • $V_0 = 0.02$ • Simulation: 30 s	Validate BOLD forward model and parameter estimation methods

3.3. **Noise-Driven Transitions Reproduce Empirical Dwell Time Distributions.** The incorporation of stochastic terms in the model (Eqs. 2.25, 2.26) enables the simulation of spontaneous transitions between metastable states. The distribution of dwell times follows a log-normal distribution (Fig. 5), with mean dwell times of 20–50 seconds consistent with empirically observed persistence times of functional network states in resting-state fMRI studies [49, 50]. These transitions are governed by Kramers' rate theory, providing a mechanistic link between microscopic neural fluctuations and macroscopic functional connectivity dynamics.

3.4. **Numerical Implementation and BOLD Signal Generation.** The spatial discretization and numerical integration methods successfully implement the full neural field model on computational grids (Fig. 6). The Balloon-Windkessel hemodynamic model transforms simulated neural activity into BOLD signals that capture the characteristic hemodynamic response function, including the delayed peak and undershoot following neural activation (Fig. 7). Parameter estimation using maximum likelihood fitting demonstrates the model's ability to capture individual differences in hemodynamic response properties.

4. Discussion

Our mathematical framework provides a comprehensive foundation for understanding the dynamical principles underlying time-varying functional connectivity in the brain. By formulating functional connectivity as a dynamical variable that co-evolves with neural activity, we bridge the gap between traditional static connectivity measures and the inherently dynamic nature of brain network interactions.

4.1. **Theoretical Advances in Modeling Brain Dynamics.** The key innovation of our approach lies in treating connectivity as a dynamical variable governed by its own evolution equation (Eq. 2.4). This departs from conventional approaches, where connectivity is typically computed as a statistical measure of correlation between time series [1,2]. Our framework captures the reciprocal relationship between neural activity and connectivity: activity patterns shape connectivity through Hebbian plasticity, while connectivity constrains the spread and integration of neural activity through network interactions.

The identification of multiple dynamical regimes monostable, bistable, and oscillatory provides a mathematical basis for understanding the diverse states of functional brain organization observed in empirical studies [21, 22]. The bistable regime, in particular, offers a mechanism for the metastability that characterizes resting-state networks, where the brain maintains flexibility to transition between different functional configurations while preserving stability within states [47].

4.2. **Biological Interpretation and Empirical Validation.** The parameters in our model map onto biologically meaningful quantities. The timescale separation parameter $\varepsilon = \alpha/\gamma$ reflects the relative speeds of neural activity dynamics and synaptic plasticity processes. The values yielding realistic dynamics ($\varepsilon \approx 0.01$–0.2) are consistent with known neurophysiological timescales, where

neural activity evolves on timescales of milliseconds while synaptic changes occur over seconds to minutes [27,30].

The noise-driven transitions between metastable states reproduce key features of empirical functional connectivity dynamics, including the log-normal distribution of dwell times and spontaneous state transitions without external input [19,49]. This suggests that stochastic fluctuations at the neural level can drive macroscopic reorganization of brain networks, providing a potential mechanism for the spontaneous cognitive processes that occur during rest.

4.3. **Relationship to Existing Computational Frameworks.** Our framework extends existing approaches in several important ways. Unlike coupled oscillator models [28] that focus on phase synchronization, our model incorporates both amplitude and connectivity dynamics. Compared to dynamic causal modeling [29], which typically assumes fixed connectivity, our approach allows connectivity to evolve dynamically based on neural activity. The neural field formulation provides spatial continuity that is lacking in discrete network models while maintaining analytical tractability through the reduced 2D system.

The Balloon-Windkessel forward model enables direct comparison with empirical fMRI data, bridging the gap between simulated neural dynamics and measured BOLD signals. This is crucial for validating model predictions against experimental observations and for estimating model parameters from empirical data.

4.4. **Limitations and Future Directions.** Several limitations of the current framework warrant attention in future work. The assumption of homogeneous neural populations could be extended to incorporate multiple neuron types with different dynamical properties. The diffusion terms in both activity and connectivity equations, while mathematically convenient, require further physiological justification regarding their biological correlates.

Future work should focus on applying the model to specific empirical questions, such as understanding connectivity dynamics in neurological and psychiatric disorders [25,26], or investigating how dynamic connectivity supports cognitive processes. The framework could also be extended to incorporate structural connectivity constraints from diffusion tensor imaging data, creating a more biologically grounded model of brain network dynamics.

Future Directions.

- Extension to heterogeneous neural populations
- Incorporation of structural connectivity constraints
- Application to clinical populations (e.g., epilepsy, Alzheimer's disease)
- Development of model-based biomarkers for disease progression

5. Conclusion

This study establishes a comprehensive mathematical framework for investigating the dynamics of functional connectivity in the brain using differential equations. By formulating a system of

coupled equations that describe the co-evolution of neural activity and functional connectivity, we provide a principled approach to understanding the time-varying nature of brain network interactions.

The key contributions of this work include:

- A novel neural field model that treats functional connectivity as a dynamical variable
- Analytical characterization of multiple dynamical regimes and bifurcations
- Demonstration of noise-driven transitions reproducing empirical dwell time distributions
- Integration with hemodynamic modeling for direct comparison with fMRI data
- Numerical implementation enabling the simulation of large-scale brain dynamics

The framework successfully captures essential features of dynamic functional connectivity, including metastability, spontaneous state transitions, and scale-invariant fluctuations. It provides testable predictions about how specific parameter changes should affect functional connectivity dynamics, offering opportunities for experimental validation.

This mathematical approach bridges multiple scales of brain organization, from local neural dynamics to large-scale network interactions, providing a foundation for understanding how the brain's functional architecture emerges from and constrains its dynamical properties. The framework offers new avenues for investigating brain dynamics in health and disease, with potential applications in basic neuroscience, clinical research, and the development of novel computational tools for analyzing brain network dynamics.

Acknowledgments: This study is supported by funding from Prince Sattam bin Abdulaziz University, project number (PSAU/2025/01/31196).

Authors' Contributions:

MTN: performed the work and analyzed the Method
MTN: wrote the manuscript

Data Availability Statement: The research presented in this manuscript is based entirely on computational simulations and mathematical modeling. No empirical datasets were collected or analyzed. All results were generated using custom Python implementations of the proposed differential equation framework. The simulation codes and parameter sets used to produce the figures and results are available from the corresponding author upon reasonable request for research purposes.

Conflicts of Interest: The author declares that there are no conflicts of interest regarding the publication of this paper.

References

[1] M.G. Preti, T.A. Bolton, D. Van De Ville, The Dynamic Functional Connectome: State-of-the-Art and Perspectives, NeuroImage 160 (2017), 41–54. https://doi.org/10.1016/j.neuroimage.2016.12.061.

[2] R.M. Hutchison, T. Womelsdorf, E.A. Allen, P.A. Bandettini, V.D. Calhoun, et al., Dynamic Functional Connectivity: Promise, Issues, and Interpretations, NeuroImage 80 (2013), 360–378. https://doi.org/10.1016/j.neuroimage.2013.05.079.

[3] A.T. Ehrlich, G. Maroteaux, A. Robe, L. Venteo, M.T. Nasseef, et al., Expression Map of 78 Brain-Expressed Mouse Orphan GPCRs Provides a Translational Resource for Neuropsychiatric Research, Commun. Biol. 1 (2018), 102. https://doi.org/10.1038/s42003-018-0106-7.

[4] M.T. Nasseef, Measuring Directed Functional Connectivity in Mouse fMRI Networks Using Granger Causality, Thesis, University of Trento, 2015.

[5] M.T. Nasseef, G.A. Devenyi, A.E. Mechling, L.A. Harsan, M.M. Chakravarty, et al., Deformation-Based Morphometry MRI Reveals Brain Structural Modifications in Living Mu Opioid Receptor Knockout Mice, Front. Psychiatry 9 (2018), 643. https://doi.org/10.3389/fpsyt.2018.00643.

[6] M.T. Nasseef, W. Ma, J.P. Singh, N. Dozono, K. Lançon, et al., Chronic Generalized Pain Disrupts Whole Brain Functional Connectivity in Mice, Brain Imaging Behav. 15 (2021), 2406–2416. https://doi.org/10.1007/s11682-020-00438-9.

[7] M.T. Nasseef, J.P. Singh, A.T. Ehrlich, M. McNicholas, D.W. Park, et al., Oxycodone-Mediated Activation of the Mu Opioid Receptor Reduces Whole Brain Functional Connectivity in Mice, ACS Pharmacol. Transl. Sci. 2 (2019), 264–274. https://doi.org/10.1021/acsptsci.9b00021.

[8] S. Ben Hamida, S. Mendonça-Netto, T.M. Arefin, M.T. Nasseef, L.J. Boulos, et al., Increased Alcohol Seeking in Mice Lacking Gpr88 Involves Dysfunctional Mesocorticolimbic Networks, Biol. Psychiatry 84 (2018), 202–212. https://doi.org/10.1016/j.biopsych.2018.01.026.

[9] L.J. Boulos, M.T. Nasseef, M. McNicholas, A. Mechling, L.A. Harsan, et al., TouchScreen-Based Phenotyping: Altered Stimulus/Reward Association and Lower Perseveration to Gain a Reward in Mu Opioid Receptor Knockout Mice, Sci. Rep. 9 (2019), 4044. https://doi.org/10.1038/s41598-019-40622-6.

[10] P. Charbogne, O. Gardon, E. Martín-García, H.L. Keyworth, A. Matsui, et al., Mu Opioid Receptors in Gamma-Aminobutyric Acidergic Forebrain Neurons Moderate Motivation for Heroin and Palatable Food, Biol. Psychiatry 81 (2017), 778–788. https://doi.org/10.1016/j.biopsych.2016.12.022.

[11] E. Fuini, A. Chang, R.J. Ortiz, T. Nasseef, J. Edwards, et al., Dose-Dependent Changes in Global Brain Activity and Functional Connectivity Following Exposure to Psilocybin: A BOLD MRI Study in Awake Rats, Front. Neurosci. 19 (2025), 1554049. https://doi.org/10.3389/fnins.2025.1554049.

[12] M. Karatas, V. Noblet, M.T. Nasseef, T. Bienert, M. Reisert, et al., Mapping the Living Mouse Brain Neural Architecture: Strain-Specific Patterns of Brain Structural and Functional Connectivity, Brain Struct. Funct. 226 (2021), 647–669. https://doi.org/10.1007/s00429-020-02190-8.

[13] D. Lupinsky, M.T. Nasseef, C. Parent, K. Craig, J. Diorio, M.J. Meaney, T.-Y. Zhang, Functional Magnetic Resonance Imaging Reveals Altered Functional Connectivity Associated with Resilience and Susceptibility to Chronic Social Defeat Stress in the Mouse Brain, Mol. Psychiatry, (in Press).

[14] S. Soltanpour, R. Utama, A. Chang, M.T. Nasseef, D. Madularu, et al., Sst-Dunet: Smart Swin Transformer and Dense UNet for Automated Preclinical fMRI Skull Stripping, J. Neurosci. Methods 423 (2025), 110545. https://doi.org/10.1016/j.jneumeth.2025.110545.

[15] M. Sourty, C. Champagnol-Di Liberti, M.T. Nasseef, L. Welsch, V. Noblet, et al., Chronic Morphine Leaves a Durable Fingerprint on Whole-Brain Functional Connectivity, Biol. Psychiatry 96 (2024), 708–716. https://doi.org/10.1016/j.biopsych.2023.12.007.

[16] M. Sourty, M.T. Nasseef, C. Champagnol-Di Liberti, M. Mondino, V. Noblet, et al., Manipulating ΔFOSB in D1-Type Medium Spiny Neurons of the Nucleus Accumbens Reshapes Whole-Brain Functional Connectivity, Biol. Psychiatry 95 (2024), 266–274. https://doi.org/10.1016/j.biopsych.2023.07.013.

[17] Y. Wang, R. Ortiz, A. Chang, T. Nasseef, N. Rubalcaba, et al., Following Changes in Brain Structure and Function with Multimodal MRI in a Year-Long Prospective Study on the Development of Type 2 Diabetes, Front. Radiol. 5 (2025), 1510850. https://doi.org/10.3389/fradi.2025.1510850.

[18] J.J. Gattuso, D. Perkins, S. Ruffell, A.J. Lawrence, D. Hoyer, et al., Default Mode Network Modulation by Psychedelics: A Systematic Review, Int. J. Neuropsychopharmacol. 26 (2022), 155–188. https://doi.org/10.1093/ijnp/pyac074.

[19] D.J. Lurie, D. Kessler, D.S. Bassett, R.F. Betzel, M. Breakspear, et al., Questions and Controversies in the Study of Time-Varying Functional Connectivity in Resting fMRI, Netw. Neurosci. 4 (2020), 30–69. https://doi.org/10.1162/netn_a_00116.

[20] B. Biswal, F. Zerrin Yetkin, V.M. Haughton, J.S. Hyde, Functional Connectivity in the Motor Cortex of Resting Human Brain Using Echo-planar MRI, Magn. Reson. Med. 34 (1995), 537–541. https://doi.org/10.1002/mrm.1910340409.

[21] D. Vidaurre, S.M. Smith, M.W. Woolrich, Brain Network Dynamics Are Hierarchically Organized in Time, Proc. Natl. Acad. Sci. U.S.A. 114 (2017), 12827–12832. https://doi.org/10.1073/pnas.1705120114.

[22] E.A. Allen, E. Damaraju, S.M. Plis, E.B. Erhardt, T. Eichele, et al., Tracking Whole-Brain Connectivity Dynamics in the Resting State, Cereb. Cortex 24 (2012), 663–676. https://doi.org/10.1093/cercor/bhs352.

[23] T. Chen, W. Cai, S. Ryali, K. Supekar, V. Menon, Distinct Global Brain Dynamics and Spatiotemporal Organization of the Salience Network, PLOS Biol. 14 (2016), e1002469. https://doi.org/10.1371/journal.pbio.1002469.

[24] P. Barttfeld, L. Uhrig, J.D. Sitt, M. Sigman, B. Jarraya, et al., Signature of Consciousness in the Dynamics of Resting-State Brain Activity, Proc. Natl. Acad. Sci. U.S.A. 112 (2015), 887–892. https://doi.org/10.1073/pnas.1418031112.

[25] E. Damaraju, E. Allen, A. Belger, J. Ford, S. McEwen, et al., Dynamic Functional Connectivity Analysis Reveals Transient States of Dysconnectivity in Schizophrenia, NeuroImage: Clinical 5 (2014), 298–308. https://doi.org/10.1016/j.nicl.2014.07.003.

[26] R.H. Kaiser, S. Whitfield-Gabrieli, D.G. Dillon, F. Goer, M. Beltzer, et al., Dynamic Resting-State Functional Connectivity in Major Depression, Neuropsychopharmacology 41 (2015), 1822–1830. https://doi.org/10.1038/npp.2015.352.

[27] M. Breakspear, Dynamic Models of Large-Scale Brain Activity, Nat. Neurosci. 20 (2017), 340–352. https://doi.org/10.1038/nn.4497.

[28] J. Cabral, M.L. Kringelbach, G. Deco, Functional Connectivity Dynamically Evolves on Multiple Time-Scales Over a Static Structural Connectome: Models and Mechanisms, NeuroImage 160 (2017), 84–96. https://doi.org/10.1016/j.neuroimage.2017.03.045.

[29] K. Friston, L. Harrison, W. Penny, Dynamic Causal Modelling, NeuroImage 19 (2003), 1273–1302. https://doi.org/10.1016/s1053-8119(03)00202-7.

[30] G. Deco, A. Ponce-Alvarez, D. Mantini, G.L. Romani, P. Hagmann, et al., Resting-State Functional Connectivity Emerges from Structurally and Dynamically Shaped Slow Linear Fluctuations, J. Neurosci. 33 (2013), 11239–11252. https://doi.org/10.1523/jneurosci.1091-13.2013.

[31] K.F. Wong, X.J. Wang, A Recurrent Network Mechanism of Time Integration in Perceptual Decisions, J. Neurosci. 26 (2006), 1314–1328. https://doi.org/10.1523/jneurosci.3733-05.2006.

[32] G. Deco, V.K. Jirsa, P.A. Robinson, M. Breakspear, K. Friston, The Dynamic Brain: From Spiking Neurons to Neural Masses and Cortical Fields, PLoS Comput. Biol. 4 (2008), e1000092. https://doi.org/10.1371/journal.pcbi.1000092.

[33] A.M. Turing, The Chemical Basis of Morphogenesis, Philos. Trans. R. Soc. Lond. Ser. B, Biol. Sci. 237 (1952), 37–72. https://doi.org/10.1098/rstb.1952.0012.

[34] M.C. Cross, P.C. Hohenberg, Pattern Formation Outside of Equilibrium, Rev. Mod. Phys. 65 (1993), 851–1112. https://doi.org/10.1103/revmodphys.65.851.

[35] J.D. Murray, ed., Mathematical Biology: II: Spatial Models and Biomedical Applications, Springer New York, New York, 2008. https://doi.org/10.1007/b98869.

[36] F.H. Fenton, E.M. Cherry, H.M. Hastings, S.J. Evans, Multiple Mechanisms of Spiral Wave Breakup in a Model of Cardiac Electrical Activity, Chaos 12 (2002), 852–892. https://doi.org/10.1063/1.1504242.

[37] M.A. Dahlem, F.M. Schneider, E. Schöll, Failure of Feedback as a Putative Common Mechanism of Spreading Depolarizations in Migraine and Stroke, Chaos 18 (2008), 026110. https://doi.org/10.1063/1.2937120.

[38] H.R. Wilson, J.D. Cowan, Excitatory and Inhibitory Interactions in Localized Populations of Model Neurons, Biophys. J. 12 (1972), 1–24. https://doi.org/10.1016/s0006-3495(72)86068-5.

[39] S. Coombes, Waves, Bumps, and Patterns in Neural Field Theories, Biol. Cybern. 93 (2005), 91–108. https://doi.org/10.1007/s00422-005-0574-y.

[40] P.C. Bressloff, Spatiotemporal Dynamics of Continuum Neural Fields, J. Phys.: Math. Theor. 45 (2011), 033001. https://doi.org/10.1088/1751-8113/45/3/033001.

[41] S. Soltanpour, A. Chang, D. Madularu, P. Kulkarni, C. Ferris, et al., 3D Wasserstein Generative Adversarial Network with Dense U-Net-Based Discriminator for Preclinical fMRI Denoising, J. Imaging Inform. Med. 38 (2025), 4196–4215. https://doi.org/10.1007/s10278-025-01434-5.

[42] H.R. Wilson, Spikes, Decisions, and Actions: The Dynamical Foundations of Neuroscience, Oxford University Press, 2006.

[43] E.M. Izhikevich, Neural Excitability, Spiking and Bursting, Int. J. Bifurc. Chaos 10 (2000), 1171–1266. https://doi.org/10.1142/s0218127400000840.

[44] C. Kuehn, Multiple Time Scale Dynamics, Springer, 2015. https://doi.org/10.1007/978-3-319-12316-5.

[45] M. Brøns, T.J. Kaper, H.G. Rotstein, Introduction to Focus Issue: Mixed Mode Oscillations: Experiment, Computation, and Analysis, Chaos 18 (2008), 015101. https://doi.org/10.1063/1.2903177.

[46] R.J. Butera, J. Rinzel, J.C. Smith, Models of Respiratory Rhythm Generation in the Pre-Bötzinger Complex. II. Populations of Coupled Pacemaker Neurons, J. Neurophysiol. 82 (1999), 398–415. https://doi.org/10.1152/jn.1999.82.1.398.

[47] E. Tognoli, J.A.S. Kelso, The Metastable Brain, Neuron 81 (2014), 35–48. https://doi.org/10.1016/j.neuron.2013.12.022.

[48] H. Kramers, Brownian Motion in a Field of Force and the Diffusion Model of Chemical Reactions, Physica 7 (1940), 284–304. https://doi.org/10.1016/s0031-8914(40)90098-2.

[49] E.C. Hansen, D. Battaglia, A. Spiegler, G. Deco, V.K. Jirsa, Functional Connectivity Dynamics: Modeling the Switching Behavior of the Resting State, NeuroImage 105 (2015), 525–535. https://doi.org/10.1016/j.neuroimage.2014.11.001.

[50] J.M. Shine, M. Breakspear, P.T. Bell, K.A. Ehgoetz Martens, R. Shine, et al., Human Cognition Involves the Dynamic Integration of Neural Activity and Neuromodulatory Systems, Nat. Neurosci. 22 (2019), 289–296. https://doi.org/10.1038/s41593-018-0312-0.

[51] A. Saltelli, M. Ratto, T. Andres, F. Campolongo, J. Cariboni, D. Gatelli, M. Saisana, S. Tarantola, Global Sensitivity Analysis. The Primer, Wiley, 2008. https://doi.org/10.1002/9780470725184.

[52] I. Sobol, Global Sensitivity Indices for Nonlinear Mathematical Models and Their Monte Carlo Estimates, Math. Comput. Simul. 55 (2001), 271–280. https://doi.org/10.1016/s0378-4754(00)00270-6.

[53] S. Soltanpour, M.T. Nasseef, R. Utama, A. Chang, D. Madularu, et al., Robust Automated Preclinical fMRI Preprocessing via a Multi-Stage Dilated Convolutional Swin Transformer Affine Registration, Front. Neurosci. 19 (2025), 1621244. https://doi.org/10.3389/fnins.2025.1621244.